Digital Object Identifier:
https://doi.org/10.1109/JPHOTOV.2019.2927918

doi.org/10.1109/JPHOTOV.2019.2927918

Understanding the AC Equivalent Circuit Response of Ultrathin $Cu(In,Ga)Se_2$ Solar Cells

J. M. V. Cunha*, C. Rocha, C. Vinhais, P. A. Fernandes and P. M. P. Salomé

***Abstract* — The present work aims to study the AC electrical response of standard-thick, ultrathin and passivated ultrathin CIGS solar cells. Ultrathin $Cu(In,Ga)Se_2$ (CIGS) is desired to reduce production costs of CIGS solar cells. Equivalent circuits for modeling the behavior of each type of solar cells in AC regime are based on admittance measurements. It is of the utmost importance to understand the AC electrical behavior of each device, as the electrical behavior of ultrathin and passivated ultrathin CIGS devices are yet to be fully understood. The analysis shows a simpler AC equivalent circuit for the ultrathin device without passivation layer, which might be explained by the lowered bulk recombination for thin film CIGS solar cells when compared with reference thick ones. Moreover, it is observed an increase in shunt resistance for the passivated ultrathin device, which strengthens the importance of passivation for shunts mitigation when compared to unpassivated devices.**

***Index Terms* — Ultrathin solar cells, admittance, passivation, $Cu(In,Ga)Se_2$**

I. Introduction

In the past years $Cu(In,Ga)Se_2$ (CIGS) thin film solar cells have increased their electrical performance significantly, yet there are several scientific and technological challenges to be studied, in particular, for ultrathin solar cells. The ultrathin devices have the potential to reduce production costs by: i) using less material and increasing machine throughput; and ii) to increase electrical performance by lowering bulk recombination [1]. Moreover, it was already shown that a nanostructured point contact layer improves the performance of ultrathin CIGS devices [1]–[5]. The improvement is due to passivation of the rear CIGS interface, as recombination in the rear contact is one of the biggest limitations of these devices. Without a rear passivation strategy, the interface of thick and ultrathin devices have the same problematics [6]. In standard thick devices, the rear recombination impact is usually not significant, as most carriers are photo-generated far from this interface and there is a Ga-gradient scheme that furthers mitigates this problem [7]. However, for ultrathin devices, the photo-generated carriers are always at a distance of a diffusion length, or less, away from the rear. So, the rear interface recombination for the same interface is very significant in this specific case. Such difference, explains the need for the introduction of a rear passivation strategy in ultrathin devices. The AC equivalent electric circuit analysis is a powerful technique used in thin film solar cells to identify and study devices electrical response. Such response depends and allows for the study of several properties, such as: electrically active defects, barrier heights, conduction channels, just to name a few. For CdTe, this technique is mostly used to study the often encountered electrical contact problem [8]–[10], the etching procedure effect [11]–[13] and doping effects [14], [15]. Furthermore, this procedure is also widely used in DSSC, perovskite, Cu_2ZnSnS_4 and silicon solar cells [16]–[23]. This technique has also been used for CIGS solar cells [24]–[28] for general defects analysis.

In this work we use AC electrical measurements to explore the effects on device performance of lowering the CIGS thickness. We present a study of standard 2000 nm thick CIGS solar cell, a 400 nm ultrathin CIGS solar cell and a 400 nm ultrathin rear passivated CIGS solar cell based on equivalent circuits to point out the most relevant electrical differences.

II. Experimental

The standard solar cell stack is: SLG/Mo/CIGS/CdS/i:ZnO/ZnO:Al with Ni/Al/Ni as front grid [29]. The CIGS layer is grown by single stage process at 550 ºC according to the process described elsewhere [29]. Three devices were studied: i) CIGS thickness of 2000 nm, hereafter named reference thick device; ii) CIGS thickness of 400 nm, henceforth entitled reference ultrathin device; and iii) rear passivated CIGS thickness of 400 nm, henceforward called passivated ultrathin device, with the following stack SLG/Mo/Al_2O_3/CIGS/CdS/i:ZnO/ZnO:Al. The CIGS thickness was measured using stylus profilometry and X-ray fluorescence (XRF). The composition of the three devices is similar: [Cu]/([Ga] + [In]) or CGI = 0.70 and [Ga]/([Ga] + [In]) or GGI = 0.295 as measured using XRF. The passivated ultrathin device has an 18 nm Al_2O_3 passivation layer, deposited by atomic layer deposition (ALD) which is crucial for the passivation effect [30]. A point contact structure was used with openings of 400 nm diameter, separated by 2 µm pitch, as it is described elsewhere [1]. We note that when a passivation layer is used, a NaF precursor layer is used as pre-deposition treatment (PDT) for Na supply due to Na blocking effect of the Al_2O_3 layer [31]. The cells were defined mechanically, which

* Corresponding author: J. M. V. Cunha (jose.cunha@inl.int).

Fundação para a Ciência e a Tecnologia (FCT) is acknowledged through: IF/00133/2015 and PD/BD/142780/2018. The European Union's Horizon 2020 research and innovation programme ARCIGS-M project (grant agreement no. 720887) is acknowledged. This research is also supported by NovaCell (028075) and InovSolarCells (029696) co-funded by FCT and the ERDF through COMPETE2020.

J. M. V. Cunha, C. Rocha, C. Vinhais, P. A. Fernandes and P. M. P. Salomé are with INL – International Iberian Nanotechnology Laboratory, Avenida Mestre José Veiga, 4715-330 Braga, Portugal (cc.rocha@campus.fct.unl.pt, carlos.vinhais@inl.int, paulo.fernandes@inl.int and pedro.salome@inl.int).

J. M. V. Cunha and P. M. P. Salomé are with Departamento de Física, Universidade de Aveiro, Campus Universitário de Santiago, 3810-193 Aveiro, Portugal.

J. M. V. Cunha and P. A. Fernandes are with I3N, Universidade de Aveiro, 3810-193 Aveiro, Portugal.

C. Vinhais is with Departamento de Física, Instituto Superior de Engenharia do Porto, Instituto Politécnico do Porto, Porto 4200-072, Portugal.

P. A. Fernandes is with CIETI, Departamento de Física, Instituto Superior de Engenharia do Porto, Instituto Politécnico do Porto, Rua Dr. António Bernardino de Almeida, 431, 4200-072 Porto, Portugal.

doi.org/10.1109/JPHOTOV.2019.2927918

consistently provides area values of 0.5 cm^2 with an error value less than 1 %. A precision LCR meter (Agilent E4890 A) was used to perform the capacitance–conductance–frequency (C-G-f) measurements at room temperature, 25 mV (V_{RMS}), 0 V_{bias} with a range of frequencies varying from 20 Hz to 1 MHz. Capacitance–voltage–frequency (C-V-f) measurements were done at room temperature, 25 mV (V_{RMS}), 10 kHz from –1 V to 0.5 V. During the measurements, device contacting was made using a series probe tip holder, with a spring gold tip directly connected to a coaxial cable to minimize cabling influence, such as series resistance and inductance elements. The measurements were performed using 2-probe configuration. Prior to the measurements, light soaking at AM1.5 during 20 minutes with cooling of the substrate to 20 ºC was performed. Completed solar cell devices were characterized by current density – voltage (J–V) measurements with AM1.5 illumination in a home-built system.

III. Procedure for the Determination of the Equivalent Circuit

The AC electrical behavior of the solar cells was modeled using ZSimpWin 3.50 software [32]. Such software uses Nonlinear Least Squares Fit principles to analyze the input impedance data and the equivalent circuit's parameters values are achieved based on the down-hill simplex method. Such method finds the global minimum of a given function, in our case, the Chi-square (χ^2) function [33]. Several equivalent circuits are tested in order to ensure the lowest fitting error while keeping circuit physical coherence for each device with different absorber thickness and considering the passivation layer. This common approach ensures that the simplest model explains the observed measurements and, for each circuit's element, a physical meaning can be established [16].

The equivalent circuit represented in Fig. 1 is considered as default by the LCR meter and it is used for measurements proposes.

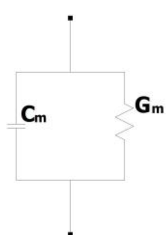

Fig. 1 - LCR meter default equivalent circuit.

The typical operation of a LCR is as follows: the measured parameters are voltage and current which are converted to values of capacitance and resistance assuming the equivalent circuit of Fig. 1. The fitting software input data is frequency, as well as, the real and imaginary parts of the circuit's impedance, represented by Z' and Z'', respectively. The equivalent circuit impedance becomes [34], [35]:

$$Z = Z' + jZ'' \Leftrightarrow Z = \frac{jRX}{R + jX} = \frac{RX^2}{R^2 + X^2} + j\frac{R^2X}{R^2 + X^2} \quad (1)$$

where R is the resistance and X is the reactance.

Considering $R = 1/G$ and $X = 1/\omega C$, the impedance of the measured equivalent circuit (a conductance, G_m, in parallel with a capacitance, C_m, as shown in Fig. 1) is represented by [34], [35]:

$$Z = \frac{j\left(\frac{1}{G_m}\right)\left(\frac{1}{\omega C_m}\right)}{\left(\frac{1}{G_m}\right) + j\left(\frac{1}{\omega C_m}\right)} \Leftrightarrow \frac{1}{Z} = G_m + j\omega C_m \quad (2)$$

where $\omega = 2\pi f$ is the angular frequency.

The fitting of a user-defined equivalent circuit to the measured data is made using advanced numerical techniques [36], through a Nyquist plot. Finally, a double Y graph is generated with the impedance amplitude and phase errors, as shown in Fig. 2.

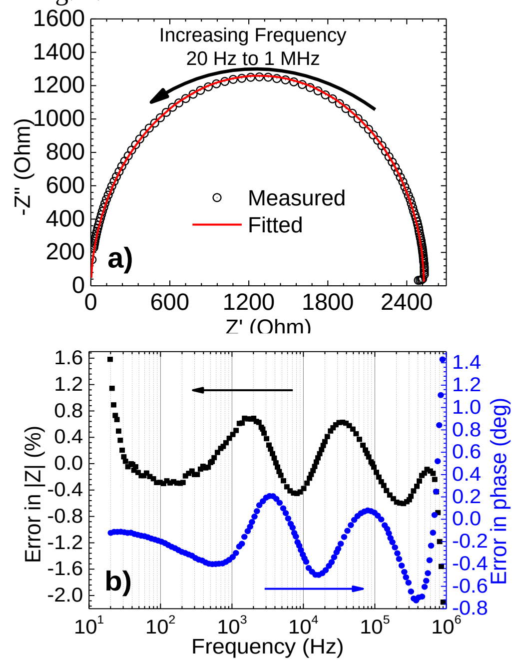

Fig. 2 - Representative: a) Nyquist plot; and b) Errors plot.

To evaluate what type of circuit is adequate, we start by testing the fitting of several circuits, which according to the literature [12], [16], [21], [22], [25] carry some physical meaning, and we carefully study the amplitude phase errors in the entire analyzed frequency spectrum. The most suitable circuit considered by us, is the one that merges both a low error together with a suitable physical meaning. This is a standard procedure in this kind of analysis [8], [12], [16]. Five individual cells of each device were analyzed, in order to have average and standard deviation values for the circuit's elements. Fig. 3 shows six equivalent circuits, although more circuits were tested, as it will be discussed. The circuits are represented each by a series resistance and nodes (parallel RC pairs) that can have several branches (series RC pairs) with capacitances and resistances. Each node/branch can model a different type of property in the solar cell such as: depletion region, non-Ohmic contacts, interface or bulk defects, barriers, just to name a few [12], [16], [20]–[22], [25]. The fundamental solar cell properties such as p-n junction and rear electrical contact (ohmic or schottky/rectifying) are generally modelled using two basic nodes: i) a representation of the depletion region by having C_{pn} as p-n junction capacitance, R_{pn} as the p-n junction resistance and R_s as series resistance [16]; and ii) a representation of the rear contact, with C_b the rear contact

doi.org/10.1109/JPHOTOV.2019.2927918

capacitance and R_b the rear contact resistance. The typical rear contact consisting of Mo/$MoSe_2$/CIGS is very complex and it is usually considered to have a small band offset (~0.2 eV) [37]–[39], which could be overcome easily at room temperature but not at low temperature [37], [38], [40] and that electrically is widely represented by a RC node like the one presented here [16], [25], [41]. The p-n junction and the rear contact nodes are distinguishable by the capacitance value, as the p-n region has a higher depletion region value than the one of rear contact. Therefore, the p-n junction capacitance has a smaller value compared to the rear contact capacitance value [12]. Moreover, a defect trap level is usually represented by a branch composed by a capacitance (C_i) and a series resistance (R_i) [12], with i = 1, 2 and 3 depending on the branch circuit position. Such series connection is due to charging/discharging time characteristic as well as electrical losses due to a defect trap level [12], [42]. However, we note that these nodes and branches, can in certain situations, be representations of other physical effects [13].

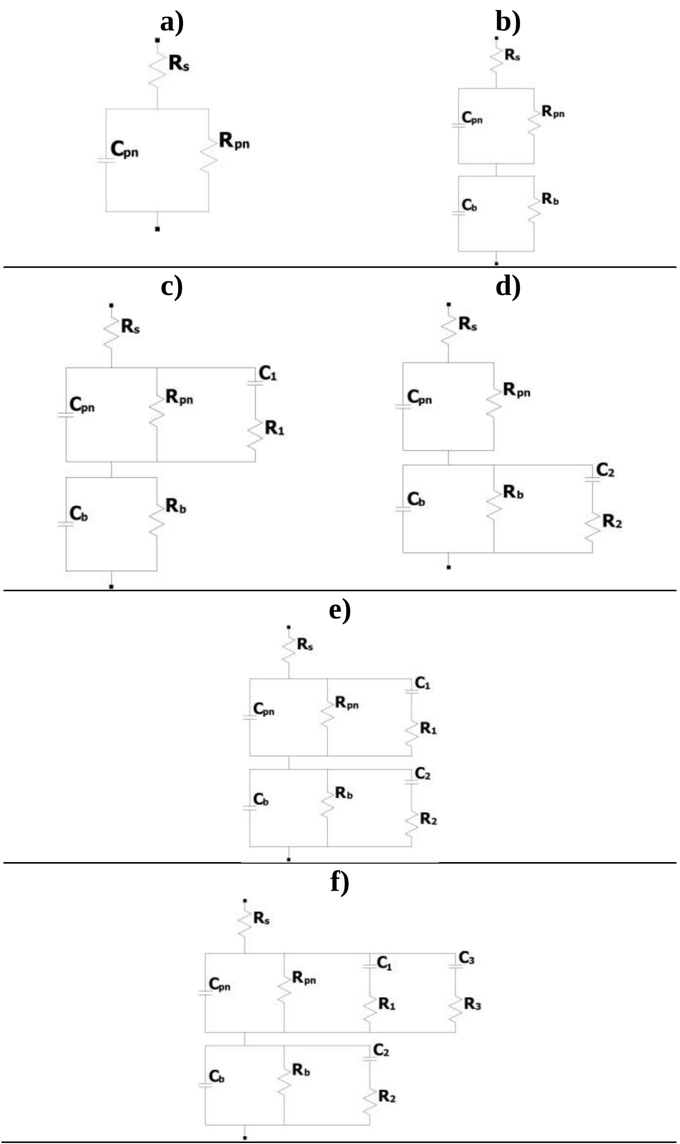

Fig. 3 - Equivalent circuits studied.

All circuits presented in Fig. 3 were also tested with an inductance in series with R_s, and we observe that the measurements setup, namely the cables, probes, tips, light soaking, just to name a few parameters, play a vital role in the measurements, which considerably affects the final result. Thus, we reach the conclusion that inductance only plays a role when non-optimized cabling is used. Due to this fact, we did not find the need to use any inductance element and we have excluded it from the presented equivalent circuits.

IV. Results and Discussion

A. J-V measurements

J-V curves are shown in Fig. 4 as well as J-V figures of merit in TABLE I. The reference thick sample has an efficiency higher than both ultrathin samples, as expected. The passivated sample clearly shows the effect of the passivation layer, as the V_{oc} has a value even higher than the one of the reference thick sample, which indicates passivation of interface defects [1]. The ideality factor (A) value close to 2 (as shown for the reference thick sample) is usually attributed to bulk recombination [43], and suggests that the bulk is playing a vital role. This fact is in agreement with the AC measurements as it will be shown later. The passivation sample has the lowest dark current density (J_0) value compared to both references, a good indication that this is the sample that suffers the least in recombination losses and in good agreement with its high V_{oc} value. Furthermore, both ultrathin samples have J_0 values lower than the thick reference, a surprising indication of lower overall recombination losses for the ultrathin samples. This point will be discussed later in the text.

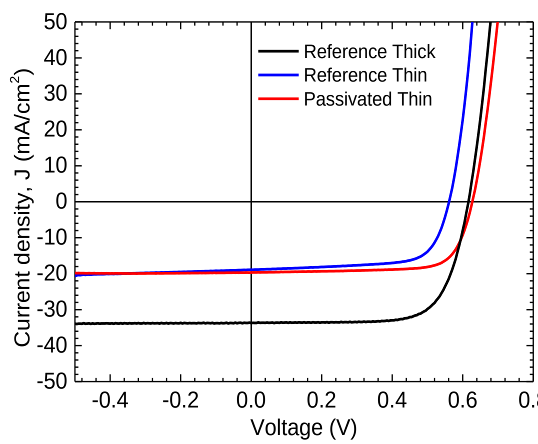

Fig. 4 – Representative illuminated J-V curves for all samples.

TABLE I
J-V FIGURES OF MERIT AVERAGES AND STANDARD DEVIATION VALUES FOR 12 SOLAR CELLS.

	V_{oc} (mV)	J_{sc} (mA/cm^2)	FF (%)	Eff (%)	A	J_0 (mA/cm^2)
Reference thick	610 ± 9	33.74 ± 0.22	72.4 ± 0.9	14.9 ± 0.4	1.76	4.53x10^{-5}
Reference ultrathin	568 ± 5	18.97 ± 0.42	70.5 ± 1.1	7.5 ± 0.3	1.32	1.28x10^{-6}
Passivated ultrathin	619 ± 10	19.80 ± 0.35	73.4 ± 1.9	9.0 ± 0.5	1.35	2.98x10^{-7}

B. AC measurements

In order to help us decide the most suitable circuit, we estimated the expected capacitance values of the p-n junction

doi.org/10.1109/JPHOTOV.2019.2927918

and of the Al_2O_3 18 nm passivation layer. The capacitance calculations were performed using the well-known capacitor equation [44]:

$$C = \frac{\varepsilon_0 \varepsilon A}{d} \quad (3)$$

where ε_0 is the vacuum permittivity, ε is the dielectric constant, A is the area and d is the width. The vacuum permittivity has a value of 8.8×10^{-12} F/m, the CIGS dielectric constant is 13.6 [45], the Al_2O_3 dielectric constant is 9 [46], the device area is 0.5 cm^2, and d is the depletion region width of the p-n junction for each device or the Al_2O_3 thickness for the passivation layer. Both net acceptors concentration (N_{cv}) and depletion region (ω) were estimated through capacitance-voltage-frequency (C-V-f) measurements. The following equations were used [47]:

$$N_{cv} = \left(\frac{-2}{\varepsilon_0 \varepsilon q A^2}\right) \times \left(\frac{dV}{d\left(\frac{1}{C^2}\right)}\right) \quad (4)$$

$$\omega = \frac{\varepsilon_0 \varepsilon A}{C} \quad (5)$$

where q is the electron charge.

The net acceptors concentration (N_{cv}) was plotted against the depletion region (ω), and as standard, the values of the depletion region were taken at 0 V (green square mark) [48], [49]. A representative curve of each sample is shown in in Fig. 5.

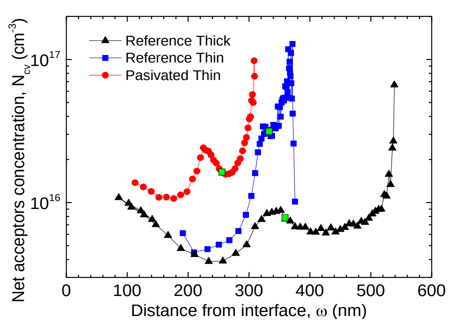

Fig. 5 – Representative plots of N_{cv} vs ω for all samples.

The N_{cv} and ω average and standard deviation values for all samples are presented in Table II.

TABLE II
N_{CV} AND ω AVERAGES AND STANDARD DEVIATION VALUES FOR ALL SAMPLES.

	ω (nm)	N_{cv} (cm^{-3})
Reference thick	362 ± 20	8.49×10^{15} ± 1.2×10^{15}
Reference ultrathin	339 ± 23	3.24×10^{16} ± 2.65×10^{15}
Passivated ultrathin	253 ± 7	1.93×10^{16} ± 3.11×10^{15}

With this approach, we reached the values shown in TABLE III, and an important observation can already be done: the capacitance of the p-n junction is an order of magnitude lower (~22-47 nF/cm^2) than the one of the passivation layer (~100 nF/cm^2). Henceforth, for the decision of circuit matching, we considered this important information.

TABLE III
EXPERIMENTAL, ESTIMATED, AND FITTED EQUIVALENT CIRCUITS' COMPONENTS. FITTED VALUES WITH AVERAGE AND STANDARD DEVIATION.

	Estimated p-n junction capacitance (nF/cm^2)	Estimated Al_2O_3 layer capacitance (nF/cm^2)	Fitted p-n junction capacitance (nF/cm^2)	Fitted Al_2O_3 layer capacitance (nF/cm^2)
Reference thick	34	N/A	22 ± 3	N/A
Reference ultrathin	36	N/A	37 ± 2	N/A
Passivated ultrathin	48	442	47 ± 1	100 ± 8

In Fig. 6, the circuit's elements averages and standard deviation values are presented for the equivalent circuit of each device and remarkably the three devices provide each, for different matched circuits.

The equivalent circuit for the reference thick device is represented by Fig. 6 a), which is in accordance with the literature [25]. The experimental average value of C_{pn} (22 nF/cm^2) is in accordance with the calculated value (34 nF/cm^2), a good indication that the matched circuit has physical meaning. For the reference ultrathin device, Fig. 6 b) shows the selected equivalent circuit, where the average C_{pn} value (37 nF/cm^2) is again in good agreement with the calculated value (36 nF/cm^2). Considering now the passivated ultrathin device shown in Fig. 6 c) with a fitted average C_{pn} value of 47 nF/cm^2, again, such value is close to the calculated one (48 nF/cm^2). For the calculated C_{pn} values, we considered an area and dielectric constant values which might be slightly different from the real layers. Hence, we consider the calculated values to be the same as the matched ones within error considerations.

The capacitance value for the passivation layer, considering a conformal and non-interrupted layer, is 442 nF/cm^2. For the circuit-extracted passivation layer capacitance (C_2) we reached an average value of 100 nF/cm^2. The difference between the calculated and the experimental values could be explained by the fact that the device passivation layer has point contacts in approximately 3 % of the area. Therefore, it is expected that the experimental passivation layer capacitance value would be lower than the calculated one. Thus, the attribution of the C_2-R_2 branch of the passivated ultrathin device, as seen in Fig. 6 c), to the Al_2O_3 layer can be justified.

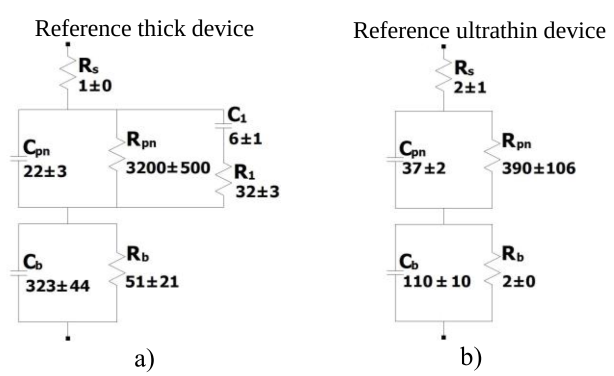

Passivated ultrathin device

doi.org/10.1109/JPHOTOV.2019.2927918

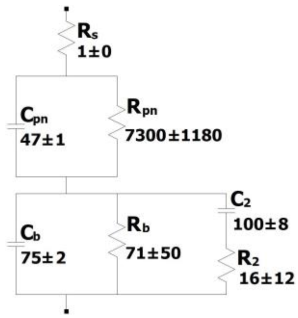

c)

Fig. 6 - Average and standard deviation element's values of selected equivalent circuits: a) reference thick device; b) ultrathin reference device; and c) passivated ultrathin device. Capacitance units are nanofarad per square centimeter (nF/cm^2) and resistance units are ohm square centimeter (Ω.cm^2).

In order to take conclusions about the shunt resistance (R_{pn}), a comparison between AC and J-V measurements was conducted, as shown in TABLE IV:

TABLE IV
RPN VALUES COMPARISON BETWEEN AC AND J-V MEASUREMENTS.

	AC R_{pn} (Ω.cm^2)	**J-V R_{pn} (Ω.cm^2)**
Reference thick	3200	1300
Reference ultrathin	390	347
Passivated ultrathin	7300	2103

The values of the AC and J-V measurements follow the same trend. Such similarity further validates the chosen models and indicates that conclusions regarding the shunt resistances from the AC measurements can be performed.

One important aspect is the low shunt resistance (R_{pn}) for the reference ultrathin device (390 Ω.cm^2) when compared with the thick one (3200 Ω.cm^2), which is indicative of more shunts for the ultrathin reference device. Such fact is typical of ultrathin devices, simply because, as the absorber layer is thinner [7], [50], the likelihood of pinholes and non-uniformities through the cell to be present are much higher. The equivalent circuit difference between the reference thick and the reference ultrathin device is the branch C_1 and R_1, which may represent additional defects in the reference thick device compared with the reference ultrathin one [12], [25]. This is a striking observation as in terms of solar cells performance, the ultrathin one is heavily limited by rear interface recombination leading to a significant lower light to power conversion efficiency (~8 %) compared with the reference thick one (~15 %). So even though intuitively one would expect the ultrathin reference device to show more recombination channels, this analysis shows otherwise. However, we must note that the measurements performed here are in the AC regime: in the solar cell standard operation, electrical transport is significantly different from the AC one. In the standard solar cell operating mode, carriers are photo-generated due to photons irradiance from the sun. The photo-generated carries rely in diffusion and electrical drifting only at CIGS/CdS due to the electrical field created by the p-n junction. Most of the photo-generated minority carriers are present only at the topmost part of the cell (CIGS/CdS), never reaching the rear contact (Mo/CIGS), as shown in Fig. 7 "solar cell standard operation". However, for AC measurements, an external electrical source is applied and responsible by the introduction and extraction of the carriers, as depicted in Fig. 7 "AC transport". Such alternate current consists at a certain instant to apply a positive charge in the rear contact pushing the holes from the rear contact through the depletion region and, at the same time, applying a negative charge in the front contact, pushing the electrons from the CdS/window layer through the depletion region. In the following instant of time, the polarization is inverted and the electrons are pulled through the window layer and the holes through the rear contact. Such polarization inversion happens with a respective frequency, which leads ultimately to the alternate current (AC) flow. In fact, as both reference devices have the same rear interface (Mo/CIGS) and in the AC measurements, carriers are driven equally to the rear interface, the representation of the rear interface should be the same. The main difference between both reference devices is in fact the available CIGS thickness layer. Assuming that both devices have the same defects density and the reference thick device has more bulk (quasi-neutral region), there will simply be a higher absolute number of defects for carriers to recombine for the reference thick device. Such aspect will increase the bulk recombination of the thick reference compared with a thinner device. Since bulk recombination can be one of the dominant loss mechanisms in standard CIGS solar cells [51]–[54], it is expected that a reduction of the thickness leads to lower bulk recombination [1], [55], [56] – this is in fact one of the arguments to develop ultrathin CIGS solar cells. Subsequently, in the reference ultrathin device, bulk defects influence are somewhat lowered by the decrease in absorber thickness. At the same time, both devices rear interfaces are the same, and these are the reasons for our interpretation of the simplest circuit of the ultrathin reference device.

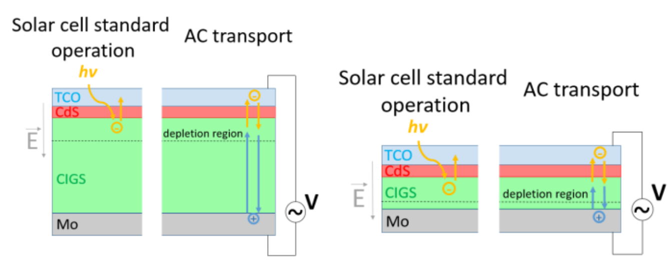

a) b)

Fig. 7 – Representation of the studied reference (not at scale) devices working in both solar cell standard operation and AC transport: a) reference thick device (2000 nm); and b) reference ultrathin device (400 nm).

When compared to the references devices, the passivated ultrathin has an extra branch located to the rear contact, and we correlate this branch to the passivation layer at the rear contact. As discussed before, there is no difference for the rear contact between both references devices. Nonetheless, the passivated ultrathin device has the dielectric layer at the rear, which will significantly change the rear contact. Such difference is also highlighted by the observed low value of rear contact capacitance, C_b. Moreover, considering the point contacts, even though they only represent approximately 3 % of the interface area, they still provide for some electrical contact, hence, here we attribute additional resistive component to the passivation layer. So, there are several indications that the extra branch of the passivated device is related with the passivation layer. Another central feature of the fitted values for the passivated ultrathin device is the increase of the shunt resistance (R_{pn}) (and to some extent of R_b as well) from 390 Ω.cm^2 to 7300 Ω.cm^2 compared to the reference ultrathin device. This increase shows that shunts particular of ultrathin devices can be mitigated by the passivation layer. This is an outstanding result, in good agreement with the literature [57], [58]. The R_{pn} average value of 7300 Ω.cm^2 (and R_b average value of 71 Ω.cm^2) are even higher than the same components values of the reference thick device, consolidating the importance of the passivation layer for shunts mitigation.

V. Conclusions

In this paper, the admittance behavior of: i) a reference thick CIGS device (standard thickness 2000 nm); ii) a reference ultrathin CIGS device (thickness 400 nm); and, iii) a passivated ultrathin device were studied. The study comprised of identifying the most suitable AC equivalent circuit that could model the experimental admittance behavior.

Surprisingly, the reference thick device, which intuitively can be considered the simplest one, does not have the simplest equivalent circuit. In fact, the AC equivalent circuit for the reference ultrathin CIGS device is the simplest one. A possible explanation for such observation is dual: i) the interfaces of both samples are the same; and ii) bulk defects play a vital role in the reference thick device, while for reference ultrathin CIGS, bulk recombination is lower. With the same effect on the rear interface for both samples and a lower bulk recombination in the reference ultrathin sample, a simpler circuit is enough to represent its AC electrical behavior. Moreover, the passivated device equivalent circuit is more complex than the ultrathin reference. We attribute the more complex circuit due to the presence of the dielectric layer at the rear contact. Furthermore, the increased number of shunts mechanisms in ultrathin devices and the potential to mitigate them using a passivation layer is well demonstrated.

This work shows that standard CIGS devices are somehow limited by the thickness of the absorber (> 2000 nm). Therefore, and according to other studies, a potential path to improve CIGS performance is to lower the standard CIGS thickness down to values around 500 nm. This thickness reduction will lower bulk recombination, allowing for higher electrical performance. Such path is only possible by introducing good passivation layers and by including light management strategies.

References

[1] P. M. P. Salomé *et al.*, “Passivation of Interfaces in Thin Film Solar Cells: Understanding the Effects of a Nanostructured Rear Point Contact Layer,” *Adv. Mater. Interfaces*, vol. 5, no. 2, p. 1701101, Jan. 2018.

[2] S. Bose *et al.*, “Optical Lithography Patterning of SiO_2 Layers for Interface Passivation of Thin Film Solar Cells,” *Sol. RRL*, vol. 2, no. 12, p. 1800212, Dec. 2018.

[3] S. Bose *et al.*, “A morphological and electronic study of ultrathin rear passivated Cu(In,Ga)Se_2 solar cells,” *Thin Solid Films*, vol. 671, pp. 77–84, Feb. 2019.

[4] G. Birant, J. de Wild, M. Meuris, J. Poortmans, and B. Vermang, “Dielectric-Based Rear Surface Passivation Approaches for Cu(In,Ga)Se_2 Solar Cells—A Review,” *Appl. Sci.*, vol. 9, no. 4, p. 677, Feb. 2019.

[5] B. Vermang *et al.*, “Employing Si solar cell technology to increase efficiency of ultra-thin Cu(In,Ga)Se_2 solar cells,” *Prog. Photovoltaics Res. Appl.*, vol. 22, no. 10, pp. 1023–1029, Oct. 2014.

[6] P. M. P. Salomé, V. Fjallstrom, A. Hultqvist, P. Szaniawski, U. Zimmermann, and M. Edoff, “The effect of Mo back contact ageing on Cu(In,Ga)Se_2 thin-film solar cells,” *Prog. Photovoltaics Res. Appl.*, vol. 22, no. 1, pp. 83–89, Jan. 2014.

[7] O. Lundberg, M. Bodegård, J. Malmström, and L. Stolt, “Influence of the Cu(In,Ga)Se_2 thickness and Ga grading on solar cell performance,” *Prog. Photovoltaics Res. Appl.*, vol. 11, no. 2, pp. 77–88, Mar. 2003.

[8] G. Friesen, M. . Özsar, and E. . Dunlop, “Impedance model for CdTe solar cells exhibiting constant phase element behaviour,” *Thin Solid Films*, vol. 361–362, pp. 303–308, Feb. 2000.

[9] Y. Y. Proskuryakov *et al.*, “Impedance spectroscopy of thin-film CdTe/CdS solar cells under varied illumination,” *J. Appl. Phys.*, vol. 106, no. 4, p. 044507, Aug. 2009.

[10] J. D. Major, Y. Y. Proskuryakov, and K. Durose, “Nucleation and Grain Boundaries in Thin Film CdTe/CdS Solar Cells,” *MRS Proc.*, vol. 1165, pp. 1165-M06-01, Jan. 2009.

[11] Y. Y. Proskuryakov, K. Durose, B. M. Taele, G. P. Welch, and S. Oelting, “Admittance spectroscopy of CdTe⁄CdS solar cells subjected to varied nitric-phosphoric etching conditions,” *J. Appl. Phys.*, vol. 101, no. 1, p. 014505, Jan. 2007.

[12] Y. Y. Proskuryakov, K. Durose, B. M. Taele, and S. Oelting, “Impedance spectroscopy of unetched CdTe/CdS solar cells—equivalent circuit analysis,” *J. Appl. Phys.*, vol. 102, no. 2, p. 024504, Jul. 2007.

[13] J. D. Major, Y. Y. Proskuryakov, and K. Durose, “Impact of CdTe surface composition on doping and device performance in close Space sublimation deposited CdTe solar cells,” *Prog. Photovoltaics Res. Appl.*, vol. 21, no. 4, pp. 436–443, Oct. 2013.

[14] Y. Y. Proskuryakov *et al.*, “Doping levels, trap density of states and the performance of co-doped CdTe(As,Cl) photovoltaic devices,” *Sol. Energy Mater. Sol. Cells*, vol. 93, no. 9, pp. 1572–1581, Sep. 2009.

[15] Y. Y. Proskuryakov *et al.*, “Comparative study of trap densities of states in CdTe⁄CdS solar cells,” *Appl. Phys. Lett.*, vol. 91, no. 15, p. 153505, Oct. 2007.

[16] P. A. Fernandes *et al.*, “Admittance spectroscopy of Cu_2ZnSnS_4 based thin film solar cells,” *Appl. Phys. Lett.*, vol. 100, no. 23, p. 233504, Jun. 2012.

[17] S. Gagliardi *et al.*, “Impedance analysis of nanocarbon DSSC electrodes,” *Superlattices Microstruct.*, vol. 46, no. 1–2, pp. 205–208, Jul. 2009.

[18] H. Rahmouni *et al.*, “Electrical conductivity and complex impedance analysis of 20% Ti-doped $La_{0.7}Sr_{0.3}MnO_3$ perovskite,” *J. Magn. Magn. Mater.*, vol. 316, no. 1, pp. 23–28, Sep. 2007.

[19] N. Shibayama, Y. Zhang, T. Satake, and M. Sugiyama, “Modelling of an equivalent circuit for Cu_2ZnSnS_4 - and $Cu_2ZnSnSe_4$ -based thin film solar cells,” *RSC Adv.*, vol. 7, no. 41, pp. 25347–25352, 2017.

[20] J. He *et al.*, “Compositional dependence of photovoltaic properties of $Cu_2ZnSnSe_4$ thin film solar cell: Experiment and simulation,” *Sol. Energy*, vol. 159, pp. 572–578, Jan. 2018.

[21] O. I. Olayiwola and P. S. Barendse, “Dynamic equivalent circuit modelling of polycrystalline silicon photovoltaic

cells," in *2017 IEEE Energy Conversion Congress and Exposition (ECCE)*, 2017, pp. 2310–2317.

[22] P. Yadav, K. Pandey, B. Tripathi, and M. Kumar, "Investigation of interface limited charge extraction and recombination in polycrystalline silicon solar cell: Using DC and AC characterization techniques," *Sol. Energy*, vol. 116, pp. 293–302, Jun. 2015.

[23] G. Oylumluoglu, A. S. Kavasoglu, and N. Kavasoglu, "The illustrated brief application of defect distribution model for heterojunction device by admittance spectroscopy," *J. Alloys Compd.*, vol. 523, pp. 16–21, May 2012.

[24] S. S. Hegedus and W. N. Shafarman, "Thin-film solar cells: device measurements and analysis," *Prog. Photovoltaics Res. Appl.*, vol. 12, no. 23, pp. 155–176, Mar. 2004.

[25] D. Tiwari *et al.*, "Single Molecular Precursor Solution for $CuIn(S,Se)_2$ Thin Films Photovoltaic Cells: Structure and Device Characteristics," *ACS Appl. Mater. Interfaces*, vol. 9, no. 3, pp. 2301–2308, Jan. 2017.

[26] T. Eisenbarth, T. Unold, R. Caballero, C. A. Kaufmann, and H.-W. Schock, "Interpretation of admittance, capacitance-voltage, and current-voltage signatures in $Cu(In,Ga)Se_2$ thin film solar cells," *J. Appl. Phys.*, vol. 107, no. 3, p. 034509, Feb. 2010.

[27] J. Kneisel, K. Siemer, I. Luck, and D. Bräunig, "Admittance spectroscopy of efficient $CuInS_2$ thin film solar cells," *J. Appl. Phys.*, vol. 88, no. 9, pp. 5474–5481, Nov. 2000.

[28] H. Bayhan and A. S. Kavasoglu, "Admittance and Impedance Spectroscopy on $Cu(In, Ga)Se_2$ Solar Cells," *Turkish J. Phys.*, vol. 27, no. 6, pp. 529–536, 2004.

[29] J. Lindahl *et al.*, "Inline $Cu(In,Ga)Se_2$ Co-evaporation for High-Efficiency Solar Cells and Modules," *IEEE J. Photovoltaics*, vol. 3, no. 3, pp. 1100–1105, Jul. 2013.

[30] J. M. V. Cunha *et al.*, "Insulator Materials for Interface Passivation of $Cu(In,Ga)Se_2$ Thin Films," *IEEE J. Photovoltaics*, vol. 8, no. 5, pp. 1313–1319, Sep. 2018.

[31] P. M. P. Salomé *et al.*, "$Cu(In,Ga)Se_2$ Solar Cells With Varying Na Content Prepared on Nominally Alkali-Free Glass Substrates," *IEEE J. Photovoltaics*, vol. 3, no. 2, pp. 852–858, Apr. 2013.

[32] B. Yeum, "Electrochemical impedance spectroscopy: Data analysis software." EChem Software, Ann Arbor, Michigan, USA, 2001.

[33] U. S. Sani and I. H. Shanono, "An Equivalent Circuit of Carbon Electrode Supercapacitors," in *Proc. 2014 Nigeria Engineering Conference*, pp. 631–639.

[34] P. A. Fernandes and P. M. P. Salomé, "Impedance spectroscopy of thin film solar cells," in *Eletrical measurements: Introduction, concepts and applications*, 2017.

[35] A. S. Kavasoglu, N. Kavasoglu, and G. Oylumluoglu, "Electrical characterization of Au/Pd/n-GaN/Pd/Au device structure in the radio frequency range by simulation study," *Synth. Met.*, vol. 161, no. 13–14, pp. 1434–1440, Jul. 2011.

[36] O. Kanoun, *Lecture Notes on Impedance Spectroscopy*. CRC Press, 2011.

[37] T. Eisenbarth, R. Caballero, M. Nichterwitz, C. A. Kaufmann, H.-W. Schock, and T. Unold, "Characterization of metastabilities in $Cu(In,Ga)Se_2$ thin-film solar cells by capacitance and current-voltage spectroscopy," *J. Appl. Phys.*, vol. 110, no. 9, p. 094506, Nov. 2011.

[38] R. Caballero *et al.*, "Impact of Na on $MoSe_2$ formation at the CIGSe/Mo interface in thin-film solar cells on polyimide foil at low process temperatures," *Acta Mater.*, vol. 63, pp. 54–62, Jan. 2014.

[39] K.-J. Hsiao, J.-D. Liu, H.-H. Hsieh, and T.-S. Jiang, "Electrical impact of $MoSe_2$ on CIGS thin-film solar cells," *Phys. Chem. Chem. Phys.*, vol. 15, no. 41, p. 18174, 2013.

[40] G. T. Koishiyev, J. R. Sites, S. S. Kulkarni, and N. G. Dhere, "Determination of back contact barrier height in $Cu(In,Ga)(Se,S)_2$ and CdTe solar cells," in *2008 33rd IEEE Photovolatic Specialists Conference*, 2008, pp. 1–3.

[41] A. Niemegeers, S. Gillis, and M. Burgelman, "Interpretation of capacitance spectra in the special case of novel thin film CdTe/CdS solar cell device structures," in *Proceedings of the 2nd World Conference on Photovoltaic Energy Conversion, JRC, European Commission, juli*, 1998, pp. 1071–1074.

[42] S. M. Sze and K. K. Ng, *Physics of Semiconductor Devices*. Hoboken, NJ, USA: John Wiley & Sons, Inc., 2006.

[43] R. Scheer, "Towards an electronic model for $CuIn_{1-x}Ga_xSe_2$ solar cells," *Thin Solid Films*, vol. 519, no. 21, pp. 7472–7475, Aug. 2011.

[44] D. K. Schroder, *Semiconductor material and device characterization*. John Wiley & Sons, 2006.

[45] A. Crovetto, M. K. Huss-Hansen, and O. Hansen, "How the relative permittivity of solar cell materials influences solar cell performance," *Sol. Energy*, vol. 149, pp. 145–150, Jun. 2017.

[46] M. J. Biercuk, D. J. Monsma, C. M. Marcus, J. S. Becker, and R. G. Gordon, "Low-temperature atomic-layer-deposition lift-off method for microelectronic and nanoelectronic applications," *Appl. Phys. Lett.*, vol. 83, no. 12, pp. 2405–2407, Sep. 2003.

[47] J. Hilibrand and R. D. Gold, "Determination of the impurity distribution in junction diodes from capacitance-voltage measurements," *RCA Rev.*, vol. 21, no. 2, pp. 245–252, 1960.

[48] P. M. P. Salome *et al.*, "Incorporation of Na in $Cu(In,Ga)Se_2$ Thin-Film Solar Cells: A Statistical Comparison Between Na From Soda-Lime Glass and From a Precursor Layer of NaF," *IEEE J. Photovoltaics*, vol. 4, no. 6, pp. 1659–1664, Nov. 2014.

[49] M. Cwil, M. Igalson, P. Zabierowski, and S. Siebentritt, "Charge and doping distributions by capacitance profiling in $Cu(In,Ga)Se_2$ solar cells," *J. Appl. Phys.*, vol. 103, no. 6, p. 063701, Mar. 2008.

[50] J. Posada, M. Jubault, and N. Naghavi, "Ultra-thin $Cu(In,Ga)Se_2$ solar cells prepared by an alternative hybrid co-sputtering/evaporation process," *Thin Solid Films*, vol. 633, pp. 66–70, Jul. 2017.

[51] R. Klenk, "Characterisation and modelling of chalcopyrite solar cells," *Thin Solid Films*, vol. 387, no. 1–2, pp. 135–140, May 2001.

[52] P. M. P. Salomé *et al.*, "A comparison between thin film solar cells made from co-evaporated $CuIn_{1-x}Ga_xSe_2$ using a one-stage process versus a three-stage process," *Prog. Photovoltaics Res. Appl.*, vol. 23, no. 4, pp. 470–478, Apr. 2015.

[53] M. A. Contreras, M. J. Romero, and R. Noufi, "Characterization of $Cu(In,Ga)Se_2$ materials used in record performance solar cells," *Thin Solid Films*, vol. 511–512, pp. 51–54, Jul. 2006.

[54] U. Rau, "Tunneling-enhanced recombination in $Cu(In, Ga)Se_2$ heterojunction solar cells," *Appl. Phys. Lett.*, vol. 74, no. 1, pp. 111–113, Jan. 1999.

[55] N. Khoshsirat, N. A. Md Yunus, M. N. Hamidon, S. Shafie, and N. Amin, "Analysis of absorber layer properties effect on CIGS solar cell performance using SCAPS," *Optik (Stuttg).*, vol. 126, no. 7–8, pp. 681–686, Apr. 2015.

[56] M. Gloeckler and J. R. Sites, "Potential of submicrometer thickness $Cu(In,Ga)Se_2$ solar cells," *J. Appl. Phys.*, vol. 98, no. 10, p. 103703, Nov. 2005.

[57] S. Garud *et al.*, "Surface Passivation of CIGS Solar Cells Using Gallium Oxide," *Phys. status solidi*, vol. 215, no. 7, p.

1700826, Apr. 2018.
[58] B. Vermang *et al.*, "Introduction of Si PERC Rear Contacting Design to Boost Efficiency of Cu(In,Ga)Se_2 Solar Cells," *IEEE J. Photovoltaics*, vol. 4, no. 6, pp. 1644–1649, Nov. 2014.